


# Modelling and optimal energy-saving control of automotive air-conditioning and refrigeration systems

Proc IMechE Part D:  
J Automobile Engineering  
2017, Vol. 231(3) 291–309  
© IMechE 2016  
Reprints and permissions:  
sagepub.co.uk/journalsPermissions.nav  
DOI: 10.1177/0954407016636978  
journals.sagepub.com/home/pid  


YanJun Huang<sup>1</sup>, Amir Khajepour<sup>1</sup>, Farshid Bagheri<sup>2</sup> and Majid Bahrami<sup>2</sup>

## Abstract

Air-conditioning and refrigeration systems are extensively adopted in homes, industry and vehicles. An important step in achieving a better performance and a higher energy efficiency for air-conditioning and refrigeration systems is a control-based model and a suitable control strategy. As a result, a dynamic model based on the moving-boundary and lumped-parameter method is developed in this paper. Unlike existing models, the proposed model lumps the effects of the fins into two equivalent parameters without adding any complexity and considers the effect produced by the superheated section of the condenser, resulting in a model that is not only simpler but also more accurate than the existing models. In addition, a model predictive controller is designed on the basis of the proposed model to enhance the energy efficiency of the air-conditioning and refrigeration systems. Simulations and experimental results are presented to demonstrate the accuracy of the model. The experiments show that an energy saving of about 8% can be achieved by using the proposed model predictive controller compared with the conventional on–off controller under the examined scenario. The better performance of the proposed controller requires electrification of the automotive air-conditioning and refrigeration systems so as to eliminate the idling caused by running the air-conditioning and refrigeration systems when a vehicle stops.

## Keywords

Control-based dynamic model, energy efficiency, model predictive controller, electrification of the automotive air-conditioning and refrigeration systems, idling

Date received: 4 November 2015; accepted: 26 January 2016

## Introduction

The continuously increasing demands on lower emission levels and better fuel economy have driven researchers to develop vehicles which are more efficient and less polluting.<sup>1</sup> However, the main auxiliary load of vehicles, the air-conditioning and refrigeration (A/C-R) systems, can consume up to 25% of the total fuel or even more in long-haul service vehicles. In addition, as the main energy consumption source in A/C-R systems, the compressor is usually connected directly to the engine via a belt in conventional vehicles, so that engines sometimes have to idle in order to power the A/C-R systems during vehicle stops. For example, long-haul trucks are equipped with a sleeper cabin where the drivers can live when they are on the road.<sup>2</sup> Usually, the trucks idle to provide power to the air-conditioning system for cabin temperature control. Similarly, food service trucks need to idle to provide power to the refrigeration system while loading or unloading. When the vehicle is idling, this gives rise to

many disadvantages, such as the low efficiency of the engine and excessive emissions.<sup>3</sup> Thus, there are significant benefits in operating A/C-R systems efficiently, in terms of both the operating costs and their effects on the environment.<sup>4</sup> An important step in achieving a better performance and a higher energy efficiency is a control-based model and an appropriate control strategy.<sup>5</sup> Therefore, making auxiliary devices more efficient can result in many benefits to vehicle owners as well as to the environment. However, in most conventional vehicles, the compressor speed is proportional to the

<sup>1</sup>Department of Mechanical and Mechatronics Engineering, University of Waterloo, Waterloo, Ontario, Canada

<sup>2</sup>School of Mechatronic System Engineering, Simon Fraser University, Surrey, British Columbia, Canada

### Corresponding author:

YanJun Huang, Department of Mechanical and Mechatronics Engineering, University of Waterloo, Waterloo, Ontario N2L3G1, Canada.  
Email: y269huan@uwaterloo.ca

engine speed instead of actively varying with the requirements of passengers or the working conditions.<sup>6</sup> This impedes development of an advanced controller for automotive A/C-R systems given that the controllers are usually applied to manipulate the speeds of the compressor and the fans. However, in the development of anti-idling technologies such as auxiliary battery-powered units, hybrid electric vehicles (HEVs) and electric vehicles (EV), the on-board energy storage system is capable of powering the A/C-R systems independently so that the A/C-R systems can be disconnected from the engines.<sup>7</sup> This means that electrification of the A/C-R systems and thus application of an advanced controller in vehicles are possible.<sup>6</sup> As a result, the idling caused by powering the auxiliary systems when the vehicle stops can be eliminated so that the performance and the efficiency of the automotive A/C-R systems is greatly improved.<sup>8</sup> This can be achieved partially by developing advanced controllers to replace the conventional on-off (bang-bang) controllers. The design of advanced controllers requires a control-based model of the A/C-R systems which is accurate but sufficiently simple for real-time implementation. A control-based model is in fact a trade-off between the accuracy and the simplicity. If the model is too simple, it is not able to reflect the main characteristics of the system, which leads to a poor closed-loop control performance. On the other hand, if it is too complex, it slows down the controller by increasing the computation time, which causes problems in real-time implementations,<sup>9</sup> although it can describe the dynamics of the system sufficiently well and produce good predictions. Consequently, this paper presents a simplified but accurate model for A/C-R systems that was validated by experimental results, and then the controllers are designed on the basis of the proposed model.

This paper is organized as follows: a literature review on the existing dynamic models of A/C-R systems is presented in the second section; next, the moving-boundary lumped-parameter model is developed. The parameters of the model are identified in the subsequent section. Then, a brief introduction of the experimental system as well as the simulations and experimental results are given for comparison and model validation. Furthermore, an on-off controller and a discrete model predictive controller are then developed, simulated, validated experimentally and compared in the next section. In the final section, comments and future work are discussed.

## Previous research

Overall, there are four main components in a vapour compression cycle: the compressor, the evaporator, the expansion valve and the condenser. The dynamics of other auxiliary components such as the accumulator and the receiver are incorporated into the connecting pipes or two heat exchangers. In the literature, the

modelling of the compressor valve and the expansion valve, irrespective of their types (electric, thermostatic or automatic expansion valves), is demonstrated by algebraic empirical equations.<sup>10</sup> This is because the dynamics of a compressor valve and an expansion valve is an order of magnitude faster than those of the heat exchangers (the evaporator and the condenser).<sup>11</sup>

Several types of model have been constructed for heat exchangers for different purposes. For example, discretized or finite difference models are more accurate and are usually used in many commercial software packages. These types of model can result in increased accuracy in prediction;<sup>12</sup> however, they are too complicated to be used in the development and implementation of a real-time control strategy. Another type of heat exchanger model is based on lumped parameters and is usually a first-order time-invariant dynamic model; however, it has oversimplified most of the dynamic characteristics of heat exchangers.<sup>13</sup> Above all, the most popular modelling approach is the moving-boundary (or moving-interface) lumped-parameter method, which is capable of reproducing the dynamics of multiple fluid-phase heat exchangers while keeping the simplicity of lumped-parameter models.<sup>13</sup> Wedekind et al.<sup>14</sup> contributed significantly by simplifying a class of two-phase transient flow problems into a type of lumped-parameter system. With experimental confirmation, they showed that the mean void fraction, i.e. the ratio of the vapour volume to the total fluid volume of the two-phase region in a heat exchanger, remains relatively unchanged. This suggests that it stays constant, irrespective of how the refrigerant is distributed throughout the heat exchanger and how the length of the two-phase region changes.<sup>11</sup> With this assumption, this method allows the two-phase section to be modelled using lumped parameters. In this way, the whole model can be much more simplified than the discretized model is. On the other hand, based on the first law of thermodynamics, the dynamics of the length of the two-phase section (the movement of the interface between different regions) can be determined.

He<sup>11</sup> used the moving-interface lumped-parameter modelling method. Based on several assumptions (e.g. that the heat exchanger is a long, thin and horizontal tube), He developed the complete non-linear dynamic model for the evaporator and the condenser, with more than five states for each of them, and then derived the entire system model by considering the boundary conditions of all the components. However, in his research, only the linearized model was partially verified.

In recent years, Alleyne and co-workers have improved the model derived by He. For instance, Li<sup>15</sup> constructed a model for the start-up period and the shutdown period by considering different distributions of the refrigerant inside the heat exchangers. Rasmussen and Alleyne<sup>13</sup> modelled the auxiliary components such as the accumulator and the receiver. Parameter identification algorithms for A/C-R system modelling have also been improved by Eldredge and

Alleyne.<sup>16</sup> Also, some special architectures for a vapour compression cycle system were modelled by Fasl.<sup>17</sup> Furthermore, the models were validated experimentally<sup>18–20</sup> and showed overall improvements with respect to the previous models. More importantly, McKinley and Alleyne<sup>21</sup> considered the effects of the fins by introducing several other parameters such as the “fraction of refrigerant-to-structure surface area on fins and refrigerant-side fin efficiency”, which makes the model more complex with nine states in the evaporator alone. In all the models above, there are more than 10 states representing the complexity of the model, which makes it difficult to guarantee the real-time running of controllers developed on the basis of these models. That is why He et al.<sup>22</sup> developed a simple model of the whole system by assuming the identical temperature of the heat exchanger wall and reduced the number of states to five. In addition, a gain-scheduling linear quadratic Gaussian technique was developed by using this simplified model. Unfortunately, the simplified model was not validated experimentally.

The disadvantages of the models existing in the literature are as follows. First, the complete models with more than 10 states are too complex to be used to develop controllers. Second, the simple model does not include the effects of the fins when modelling heat exchangers, which results in discrepancies in the model. As a result, this paper is intended to improve further the accuracy of the model reported by McKinley and Alleyne<sup>21</sup> by incorporating the fins in the model of the heat exchangers in a new way without adding to the complexity of the model. The proposed model is validated experimentally and compared with the existing model.

In this paper, an advanced model predictive controller is designed for the A/C-R systems for HEVs, EVs and conventional vehicles with auxiliary battery-powered units, where the A/C-R systems can be directly powered by the on-board energy storage system. First, a simplified control-oriented dynamic model of the automotive A/C-R systems is developed, where only six states instead of more than 10 states as reported in the literature are used. In order to keep the accuracy of this simplified model comparable with those of high-order models, the effects of the fins are considered and lumped into two equivalent parameters. In addition, the effect of the superheated section of the condenser is also included in the model by studying the experimental data instead of the model used by McKinley and Alleyne.<sup>21</sup> This model is simulated and experimentally validated for several scenarios. The results show that this model is simple and sufficiently accurate to be used in real-time control systems. Using this model, an energy-saving model predictive controller is designed, and its performance is compared with that of the conventional on-off controller. Because of some discrete constraints, this model predictive controller is designed as a discrete model predictive controller, which is seldom mentioned in the existing literature. In addition,

since operation of the A/C-R systems increases the fuel consumption by 90% at the maximum during vehicle idling,<sup>23</sup> this work is an important step in developing anti-idling technologies for conventional vehicles. For example, the better performance and the higher energy efficiency of the proposed model predictive controller can require electrification of the automotive A/C-R systems so as to reduce vehicle idling. Furthermore, this fast and robust model predictive controller can always guarantee the minimum power consumption for A/C-R systems under any working conditions. Because of the relatively slow dynamics of the working conditions of A/C-R systems, this slowly changing power consumption information can be integrated into a power management strategy as the auxiliary power taken out of the energy storage system<sup>24</sup> for prediction of the state of charge to enhance the overall efficiency of the HEVs and EVs.

## Model

An A/C-R system cycle or a vapour compression cycle generally consists of four main components, as shown in Figure 1, where the evaporator and condenser are divided into several sections under normal working conditions. There are two sections (i.e. the two-phase section and the superheated section) in the evaporator and three sections (i.e. the superheated section, the two-phase section and the subcooling section) in the condenser. The valve is used to maintain the pressures of the two heat exchangers, while the compressor sends the refrigerant from the low-pressure heat exchanger to the high-pressure heat exchanger.

The working principle of the A/C-R systems is briefly described below. The refrigerant before entering the evaporator is characterized by the low-pressure low-temperature two-phase state. In the evaporator, it absorbs heat from the specific space and changes into the vapour phase after exiting from the evaporator. The vapour refrigerant is compressed by the

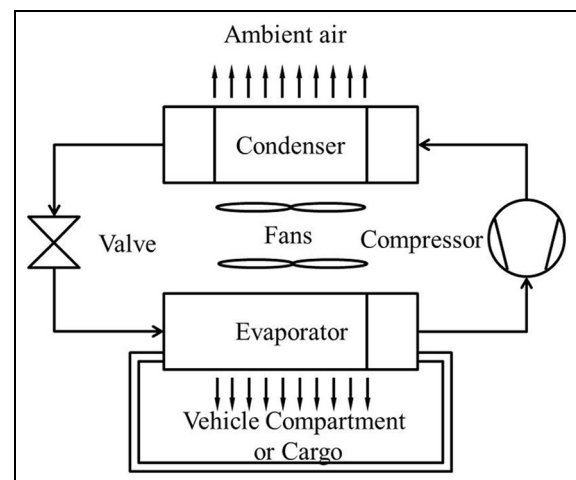


Figure 1. Schematic diagram of the A/C-R systems.

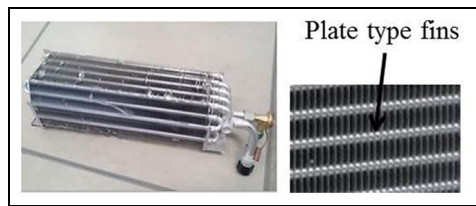


Figure 2. Fin-tube type evaporator with plate fins.

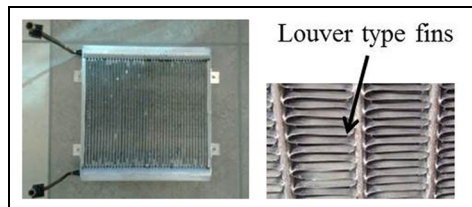


Figure 3. Microchannel type condenser with louvre fins.

compressor and turned into high-pressure high-temperature vapour. It is then sent to the condenser where the removal of its heat results in a high-pressure low-temperature liquid phase. Finally, after going through the expansion valve, the pressure drops to the evaporator pressure, and the liquid refrigerant is changed into the two-phase state. The same cycle is repeated again.

As is well known, the dynamics of the valve and the compressor are so fast with respect to the cooling process that they can be treated by some empirical equations obtained from test data. However, for the two heat exchangers (the evaporator and the condenser), owing to their complex nature, the moving-boundary lumped-parameter modelling method is employed to develop their control-based dynamic model.

In the vapour compression system modelled and experimentally validated in this work, the expansion valve is a thermostatic expansion valve, which adjusts its degree of opening according to the refrigerant temperature (the superheat temperature) at the outlet of the evaporator. The evaporator is a fin-tube type, and the condenser is a microchannel type, as shown in Figure 2 and Figure 3 respectively. The refrigerant used is R134a.<sup>25</sup> This section presents only the main dynamic equations. For the complete version of the non-linear and linearized model for development of the model predictive controller, see Appendix 2.

### Thermostatic expansion valve

The expansion valve is assumed to be isenthalpic, i.e. the enthalpy at the valve inlet is identical with that at the valve outlet.<sup>16</sup> The other important parameter is the refrigerant mass flow rate  $\dot{m}_v$  through the expansion valve which is modelled by

$$\dot{m}_v = C_v A_v \sqrt{\rho_v (P_c - P_e)} \quad (1)$$

where  $P_c$  is the pressure of the condenser,  $P_e$  is the pressure of the evaporator,  $\rho_v$  is the density of the refrigerant at the valve inlet,  $C_v$  is the discharge coefficient (which is mapped as a polynomial correlation ( $C_v = f_c(P_c - P_e)$ ) of the pressure difference between the evaporator and the condenser) and  $A_v$  is the area of the valve opening (which is mapped as a polynomial correlation ( $A_v = f_A(P_{sat} - P_e)$ ) of the pressure difference between the evaporator and the saturation pressure of the evaporator outlet temperature). These correlations can be obtained from experimental data. The remaining parameters such as the density can be obtained from the thermodynamic properties<sup>25</sup> of the refrigerant which have been compiled in look-up tables.

### Compressor model

The dynamics of the compressor can be described by

$$\dot{m}_{comp} = N_{comp} V_d \eta_{vol} \rho_{ref}(P_e) \quad (2)$$

$$h_{oc} = \eta_a [h_{is}(P_e, P_c) - h_{ic}(P_e)] + h_{ic}(P_e) \quad (3)$$

where  $\dot{m}_{comp}$  is the refrigerant mass flow rate through the compressor,  $N_{comp}$  is the compressor speed,  $V_d$  is the volumetric displacement of the compressor,  $\rho_{ref}$  is the density of the refrigerant inside the compressor,  $h_{oc}$  is the enthalpy at the compressor outlet,  $h_{ic}$  is the enthalpy at the compressor inlet,  $h_{is}(P_e, P_c)$  is the isentropic enthalpy during the compression process, which can be found from the thermodynamic properties of the refrigerant,  $\eta_{vol}$  is the volumetric efficiency (which can be obtained from the polynomial correlation  $\eta_{vol} = f_{vol}(N_{comp}, P_c - P_e)$  with respect to the speed of compressor and the two pressures) and  $\eta_a$  is the adiabatic efficiency (which can be obtained from the polynomial correlations  $\eta_a = f_a(N_{comp}, P_c - P_e)$  with respect to the speed of compressor and the two pressures).<sup>13,16,26</sup>

### Fin-tube-type evaporator

Basically, two common types of heat exchanger are used in A/C-R systems: the fin-tube type and the microchannel type. In the experimental system in this study, the fin-tube-type evaporator as seen in Figure 2 is used.

Under normal working conditions, the evaporator can be divided into two sections: the two-phase section and the superheated section. The modelling is based on the whole heat transfer process: the heat convection between the refrigerant inside the evaporator tube and the tube wall and fins, the heat conduction throughout the tube wall and fins, and the heat convection between the tube wall and fins and the ambient fluid-like air. This process is applied to the two sections. Based on the energy conservation of the heat transfer process and the mean void fraction concept mentioned in the previous section, the dynamic equations for each section can be obtained. Furthermore, the whole heat

exchanger model can be developed by considering the boundary conditions between different sections.<sup>9,10</sup>

All the heat exchanger models in the literature are based on the assumption of a long thin one-dimensional tube. They do not consider the effects of the fins or consider them in a complicated way<sup>18</sup> when modelling the heat convection between the tube wall and the refrigerant inside. However, from Figure 2 and Figure 3, it can be seen that there are many fins (plate type or louvre shape type) around the tube walls. Usually the fins and the tubes are made from the same material. If the heat conduction throughout the fins is not considered, this introduces inaccuracy into the model.

Unlike the thin tube wall where no temperature gradient is assumed, the fins are long, and a one-dimensional temperature gradient exists along the length of the fins. This gradient is dependent on the structure of the fins and is difficult to simulate. However, from the perspective of energy conservation, the energy transferred from the refrigerant to the tube wall and fins is identical with the energy taken away by the air and the energy kept in the wall and fins because of their thermal inertia. In this way, the wall and the fins can be lumped together, as shown in the dashed rectangle in Figure 4. Thus, it is reasonable to utilize an equivalent temperature  $T_{wfe}$  to represent the temperature of the wall and the fins. The other equivalent parameter used is the refrigerant-side heat transfer coefficient. In the evaporator,  $\alpha_{ie}$  and  $\alpha_{iesh}$  are the coefficient for the two-phase section and the coefficient for the superheated section respectively. After applying these equivalent parameters, the simplified non-linear dynamic model of the evaporator can be written as<sup>11,22</sup>

$$h_{lge}\rho_{le}(1 - \bar{\gamma}_e)A_e \frac{dl_e}{dt} = \dot{m}_v(h_{ge} - h_{ie}) - \alpha_{ie}\pi D_{ie}l_e(T_{wfe} - T_{re}) \quad (4)$$

$$A_e L_e \frac{d\rho_{ge}}{dP_e} \frac{dP_e}{dt} = \dot{m}_v \frac{h_{ie} - h_{le}}{h_{lge}} - \dot{m}_{comp} + \frac{\alpha_{ie}\pi D_{ie}l_e(T_{wfe} - T_{re})}{h_{lge}} \quad (5)$$

$$(C_p m)_{wfe} \frac{dT_{wfe}}{dt} = \alpha_{oe} A_{oe} (T_{ae} - T_{wfe}) - \alpha_{ie}\pi D_{ie}l_e(T_{wfe} - T_{re}) - \alpha_{iesh}\pi D_{ie}(L_e - l_e)(T_{wfe} - T_{re}) \quad (6)$$

where the three states refer to the length  $l_e$  of the two-phase section, the pressure  $P_e$  of the evaporator and the equivalent temperature  $T_{wfe}$  of the tube wall and the fins. Equation (4) simulates the energy transfer from the refrigerant to the heat exchanger tube wall and the fins of the two-phase section. The first term on the right-hand side of this equation shows the energy change after the refrigerant goes through the two-phase section, where  $h_{ge}$  is the enthalpy of the vapour refrigerant under the current pressure, or the enthalpy at the boundary of the two sections, and  $h_{ie}$  is the enthalpy of the refrigerant at the evaporator inlet. The second term describes the energy absorbed from the evaporator tube wall and the fins of the two-phase section, where  $D_{ie}$  is the inner diameter of the tube and  $T_{re}$  is the saturation temperature of the refrigerant under the current pressure. Thus, the difference between these two terms represents the energy absorbed or rejected by the two-phase section or the energy needed to evaporate the liquid refrigerant in the two-phase section. From this energy change, the two-phase length change can be obtained by using the left-hand side term, where  $h_{lge}$  is the latent enthalpy,  $\rho_{le}$  is the liquid refrigerant density,  $1 - \bar{\gamma}_e$  is the liquid volumetric fraction of the two-phase section and  $A_e$  is the sectional area of the tube.<sup>18</sup> All the enthalpies  $h_{ge}$ ,  $h_{ie}$  and  $h_{lge}$ , the densities  $\rho_{le}$ ,  $\rho_{ge}$  and  $\rho_{ie}$ , the density variation  $d\rho_{ge}/dP_e$  with respect to the pressure and the temperature  $T_{re}$  of the refrigerant can be obtained from the thermodynamic properties<sup>25</sup> of the used refrigerant which have been compiled in look-up tables; the heat transfer coefficients are identified by experimental data and shown in Table 1.

Equation (5) denotes the vapour refrigerant change rate throughout the evaporator tube. The first term on the right-hand side of this equation refers to the vapour mass at the evaporator inlet. As is known, the refrigerant becomes a two-phase refrigerant after going

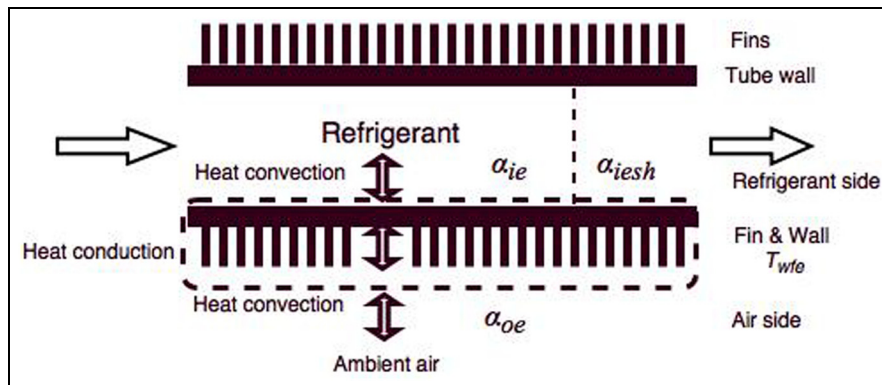


Figure 4. Schematic diagram of the evaporator with the equivalent parameters.



**Table 1.** The known and identified parameters at one steady state.

| Known parameter (units) | Value | Identified parameter (units)          | Value  |
|-------------------------|-------|---------------------------------------|--------|
| $N_{comp}$ (r/min)      | 4500  | $l_e$ (m)                             | 2.0137 |
| $N_{evap}$ (Hz)         | 41.3  | $l_c$ (m)                             | 0.2528 |
| $N_{cond}$ (Hz)         | 52.5  | $T_{wfe}$ (°C)                        | 3.84   |
| $T_{e\_air\_in}$ (°C)   | 20    | $T_{wfc}$ (°C)                        | 33.9   |
| $T_{c\_air\_in}$ (°C)   | 27    | $\alpha_{ie}$ (kW/m <sup>2</sup> K)   | 0.68   |
| $P_e$ (bar)             | 2.23  | $\alpha_{ic}$ (kW/m <sup>2</sup> K)   | 1.9    |
| $P_c$ (bar)             | 8.95  | $\alpha_{iesh}$ (kW/m <sup>2</sup> K) | 0.045  |
| $T_{sh}$ (°C)           | 2.74  | $\alpha_{ics}$ (kW/m <sup>2</sup> K)  | 0.13   |

through the expansion valve liquid. Based on the enthalpy  $h_{ie}$  of the refrigerant, the liquid enthalpy  $h_{le}$  and the latent enthalpy  $h_{lge}$ , the liquid percentage at the evaporator inlet can be found. The second term represents the mass flow rate leaving the evaporator, whereas the third term represents the vapour refrigerant which has changed from liquid. The left-hand side is the vapour mass change rate inside the evaporator. The pressure change rate can be found via the density change rate by using the chain rule, where  $L_e$  is the total length of the evaporator tube wall and  $\rho_{ge}$  is the density of the vapour refrigerant under the current evaporator pressure  $P_e$ .

Equation (6) reflects the heat conduction of the whole heat transfer process. The first term on the right-hand side refers to the total energy transferred to the tube wall and the fins from the ambient air, where  $\alpha_{oe}$  is the heat transfer coefficient, which can be found from the Colburn  $j$ -factor correlation,  $A_{oe}$  is the total outside area of the tube wall as well as the fins and  $T_{ae}$  is the mean air temperature. The last two terms are the energy transferred from the tube wall and the fins to the refrigerant in the two-phase section and the superheated section respectively, where  $\alpha_{iesh}$  is the heat transfer coefficient in the superheated section. The left-hand side shows the change in the temperature of the tube wall and the fins, where  $m$  is the total mass of the tube wall and the fins and  $C_p$  is the specific heat of the tube wall and the fins.

Since the equivalent temperature of the wall and the fins is defined on the basis of energy conservation, it is not the temperature of the wall or the fins, and so it cannot be measured directly. After lumping the fins and the wall together, the Pierre correlation<sup>11</sup> for calculating the refrigerant-side heat transfer coefficient is no longer suitable. However, these equivalent parameters can be identified easily from equations (5) and (6).

### Microchannel-type condenser

As mentioned above, the microchannel-type condenser is modelled and used in the experimental work. It can be seen from Figure 3 that there are many louver-shaped fins around each tube. There are many parallel

microchannels inside each tube. Under normal working conditions, the refrigerant distribution is more complex than that of the evaporator.

The condenser can be divided into three sections; however, in order to simplify the model for the purpose of real-time application, study of the experimental data suggests that the subcooling section could be neglected because of the much lower subcooling temperature (about 2 °C) compared with the superheat temperature (about 50 °C). Another reason is that the energy rejected to generate this lower subcooling temperature is also relatively small. Also, the small energy error caused can be compensated by the equivalent heat transfer coefficient of the two-phase section. To make up for this subcooling section from a temperature viewpoint, the refrigerant temperature at the condenser outlet can be found from experimental data. Using the above assumptions, the condenser equations can be obtained in a similar manner to the evaporator equations.

It is known that the total mass  $m_{total}$  of the refrigerant inside the cycle is constant without considering the leakage. The mass of refrigerant outside the two heat exchangers is defined as  $m_{pipe}$ . Therefore, the difference between these two masses represents the mass inside the evaporator and the condenser, which can be obtained from<sup>13</sup>

$$m_{total} - m_{pipe} = A_e [\rho_{le} l_e (1 - \bar{\gamma}_e) + \rho_{ge} l_e \bar{\gamma}_e + \rho_{she} (L_e - l_e)] + A_c [\rho_{lc} l_c (1 - \bar{\gamma}_c) + \rho_{gc} l_c \bar{\gamma}_c + \rho_{shc} (L_c - l_c)] \quad (7)$$

The first term on the right-hand side refers to the refrigerant mass of both the vapour and the liquid inside the evaporator, and the second term to that inside the condenser, where  $l_c$  is the length of the two-phase section of the condenser and  $\bar{\gamma}_c$  is the mean void fraction of the two-phase section of the condenser. Therefore, from equations (4) and (7), the two-phase length of condenser can be found. As a result, there are only two states, namely the pressure  $P_c$  and the equivalent temperature  $T_{wfc}$ , which can be used to write the condenser equations similar to the the evaporator equations<sup>22</sup> according to

$$A_c L_c \frac{d\rho_{gc}}{dP_c} \frac{dP_c}{dt} = \dot{m}_{comp} - \frac{\alpha_{ic} \pi D_{ic} l_c (T_{rc} - T_{wfc})}{h_{lge}} \quad (8)$$

$$(C_p m)_{wfc} \frac{dT_{wfc}}{dt} = \alpha_{oc} (N_{cond}) A_{oc} (T_{ac} - T_{wfc}) - \alpha_{ic} \pi D_{ic} l_c (T_{wfc} - T_{rc}) - \alpha_{ics} \pi D_{ic} (L_c - l_c) \left( T_{wfc} - \frac{T_{rc} + T_{ic}}{2} \right) \quad (9)$$

The meanings and acquisition methods of all the parameters used in the above equations are similar to those utilized in the explanations of equation (5) and equation (6).

## Pipes

In the vapour compression cycle, the four main components are connected by several pipes of different sizes. Usually, the pipes are assumed to be adiabatic, and the pressure loss is neglected because of the short length. The refrigerant mass inside the pipe is  $m_{pipe}$ , and it is estimated from the length and the inner diameter of each piece of pipe. Using the pressure inside the pipe, the density is found. The state of the refrigerant in each pipe is assumed to be uniform except for the pipe between the expansion valve and the evaporator, where the refrigerant is in the two-phase state. The vapour percentage can be approximated by  $(h_{ie} - h_{le})/h_{lge}$ , as explained in the evaporator model.

## Parameter estimation

In the vapour compression cycle model, there are three kinds of parameter: physical parameters, empirical parameters and identified parameters.

### Physical parameters

The physical parameters such as the dimensions of the pipes, the lengths, the inner and outer diameters and the interior and exterior areas of the heat exchangers can be easily measured or obtained from the manufacturers.

### Empirical parameters

Empirical parameters can be estimated by empirical equations obtained from the experimental data. Most of these parameters vary with the working conditions. Therefore, each parameter should be calculated online to update its value. For each parameter, several correlations may exist. In the following section, the mean void fraction and the air-side heat transfer coefficient are discussed in more detail.

**The mean void fraction  $\bar{\gamma}$ .** The mean void fraction  $\bar{\gamma}$  is defined as the ratio of the vapour volume to the total volume in the two-phase region and has been employed to describe the characteristics of the two-phase flows.<sup>16</sup> Wedekind et al.<sup>14</sup> mentioned that the mean void fraction can be assumed to be constant during transient processes. However, recently this parameter has been assumed to change with the fluid quality; it is defined as the ratio of the vapour mass to the total mass entering the heat exchangers and is calculated from<sup>15,19</sup>

$$\bar{\gamma} = \frac{1}{\beta} + \frac{1}{x_2 - x_1} \left[ \frac{\alpha}{\beta} \ln \left( \frac{\beta x_1 + \alpha}{\beta x_2 + \alpha} \right) \right] \quad (10)$$

with

$$\alpha = \frac{\rho_g}{\rho_f} S, \beta = 1 - \alpha$$

where  $S$  is the slip ratio defined as the ratio of the vapour velocity to the liquid velocity in the two-phase sections and is identified by test data,  $x_1$  is the fluid quality at the inlet of the two-phase section and  $x_2$  is the fluid quality at the outlet of the two-phase section.

**Air-side heat transfer coefficient  $\alpha_o$ .** The air-side heat transfer coefficient is related to the energy transferred from the heat exchanger tube wall and fins. However, for different kinds of fin, there are different empirical correlations. In this study, the Colburn  $j$  factor is used, which provides a way of relating the Reynolds number of air flow through a heat exchanger to the experimentally determined heat transfer characteristics of the heat exchanger.<sup>13,17</sup> The air-side heat transfer coefficient can be found from the  $j$  factor by using

$$j = St Pr^{2/3} \quad (11)$$

where the Colburn  $j$  factor is related to the Reynolds number and the physical structure of the heat exchanger. For the fin-tube-type evaporator, see the paper by Nejad et al.<sup>27</sup> and, for the microchannel condenser, see the paper by Jabardo and Mamani.<sup>28</sup> The Prandtl number  $Pr$  is calculated at air temperature; the Stanton number<sup>13</sup>  $St$  is related to the air-side heat transfer coefficient and is defined by

$$St = \frac{\alpha_o}{GC_p} \quad (12)$$

where  $G$  is the air mass flux across the heat exchanger and  $C_p$  is the thermal conductivity of air at the air temperature. By reconstructing the above two equations, the heat transfer coefficient becomes

$$\alpha_o = \frac{jGC_p}{Pr^{2/3}} \quad (13)$$

**Mean air temperature  $T_a$  around the heat exchangers.** This parameter can be assumed to be the mean temperature of the air temperature at the inlet and the outlet of the heat exchanger.<sup>13</sup> Taking the evaporator as an example, in order to find the air temperature at the outlet of the heat exchanger,  $T_{ae}$  should first be calculated from

$$T_{ae} = \left[ 2 \left( \frac{\dot{m}_{air-e} C_{p,air}}{\alpha_{oe} A_{oe}} \right) T_{a,in} + T_{wfe} \right] / \left[ 2 \left( \frac{\dot{m}_{air-e} C_{p,air}}{\alpha_{oe} A_{oe}} \right) + 1 \right] \quad (14)$$

where  $\dot{m}_{air-e}$  is the air mass flow rate going through the evaporator and  $C_{p,air}$  is the specific heat of the air. In this process,  $\dot{m}_{air-e}$  is proportional to the control signal  $N_{evap}$  of the evaporator fan. This proportional coefficient can be identified by using experimental data.  $T_{ac}$  at the condenser side can be calculated in a similar manner.  $T_{a,in}$  is the air temperature at the evaporator inlet and is measured by thermocouples.

### Identified parameters

Identified parameters, such as the equivalent refrigerant-side heat transfer coefficients and the equivalent temperature of the wall and the fins, refer to the parameters that are obtained from experimental data. Regarding the steady-state test for parameter identification, the system is fed by the three inputs and the two temperatures shown in the column of known parameters in Table 1. After running for about 30 min, the system approaches the steady state. The data on the temperatures, the pressures and the refrigerant mass flows are collected by using the sensors mentioned in the section on experiments and model validation. The parameters and states in the column of identified parameter are identified offline by using the least-squares method based on the collected data.

The known parameters include the inputs of the system, the working conditions and the measurements, whereas the identified parameters consist of the immeasurable states and the refrigerant-side heat transfer coefficients. Here, the equivalent two-phase heat transfer coefficient  $\alpha_{ie}$  for the evaporator is described in detail. From Table 1, this parameter for the evaporator is  $0.68 \text{ kW/m}^2 \text{ K}$ , whereas the reported value in the literature is usually between  $1 \text{ kW/m}^2 \text{ K}$  and  $5 \text{ kW/m}^2 \text{ K}$ . This is because, after considering the effects of the fins, the identified equivalent temperature  $T_{wfe}$  of the tube wall and the fins becomes higher than the temperature of the exact tube wall at the evaporator side. The temperature difference  $T_{wfc} - T_{rc}$  from the refrigerant saturation temperature at the current pressure is also larger. In order to balance the transferred energy  $\alpha_{ie} \pi D_i l_e (T_{wfc} - T_{rc})$  of the two-phase section, the equivalent heat transfer coefficient must be smaller than that estimated by the Pierre empirical correlation.<sup>19</sup> As a result, this coefficient is called the equivalent coefficient; the equivalent heat transfer coefficient for the condenser can be obtained in a similar way.

### Implementation and simulations

By considering the boundary conditions of the components (e.g. the temperature and the enthalpy at the evaporator outlet are identical with the temperature and the enthalpy respectively at the compressor inlet), the whole cycle can be simulated using the above model (equations (1) to (14)). In this model, the inputs are the compressor speed  $N_{comp}$ , the control frequency  $N_{evap}$  of the evaporator fan and the control frequency  $N_{cond}$  of the condenser fan (the latter two are proportional to the two respective fan speeds). The air temperature  $T_{e\_air\_in}$  at the evaporator inlet and the air temperature  $T_{c\_air\_in}$  at the condenser inlet are assumed to be measured and known. The five model states are the pressure  $P_e$  of the evaporator, the pressure  $P_c$  of the condenser, the two-phase section length  $l_e$ , the equivalent tube wall and fin temperature  $T_{wfe}$  of the evaporator and the equivalent tube wall and fin temperature  $T_{wfc}$  of the

condenser. Many outputs can be calculated by this model, including the air temperature at the evaporator outlet, which is related to the cooling capacity of the system. The initial conditions and parameters were estimated offline by using steady-state test data. The model was constructed in MATLAB/Simulink.

### Experiments and model validation

In this section, the experimental system is briefly introduced, and then the model validation work is carried out under different scenarios.

#### Experimental system

In order to verify the developed model, an experimental system provided by one of the industrial partners used for a truck is constructed to simulate the real operating conditions of the A/C-R systems. The schematic diagram of the whole experimental set-up is shown in Figure 5, where the condenser-side environmental chamber can provide air at any desired temperature and humidity for the condenser to simulate the ambient temperature. The evaporator and condenser units are connected by pipes via a thermostatic valve and compressor to two environmental chambers.

In order to identify and validate the proposed simplified model, many sensors are installed at different locations for measurement. A transmitter (Micro Motion 2400Sr with 0.5% accuracy from Emerson Electric Co.) is utilized to log the refrigerant mass flow rate, and it is located between the condenser and the thermostatic expansion valve. T-type thermocouples and pressure transducers (model PX309 manufactured by OMEGA with 0.25% accuracy) are installed on four locations of the whole system to measure both the high and low temperatures and the high and low pressures respectively of the refrigerant. Other T-type thermocouples and a wind sensor (model MD0550 from Modern Device) are installed at eight locations on the evaporator and condenser air streams. Also, a National Instruments (NI) data acquisition system (NI CompactDAQ eight-slot USB chassis) is employed to collect data from the thermocouples, the pressure transducers, the d.c. power supply and the flow meters and to send them to a computer. LabVIEW software is employed to obtain all the measured data from the equipment and to save them in an Excel file.

The two fans of the evaporator and condenser are controlled by two variable-frequency drives from Yaskawa (GPD 315/V7) such that the speed can be represented by the frequency. As the compressor has only three different speeds, a NI relay module (NI 9485) is used to switch between the three discrete speeds.

#### Model validation

Using the experimental set-up, different experiments are conducted; some are used for parameter identifications and the rest for model validation. For the



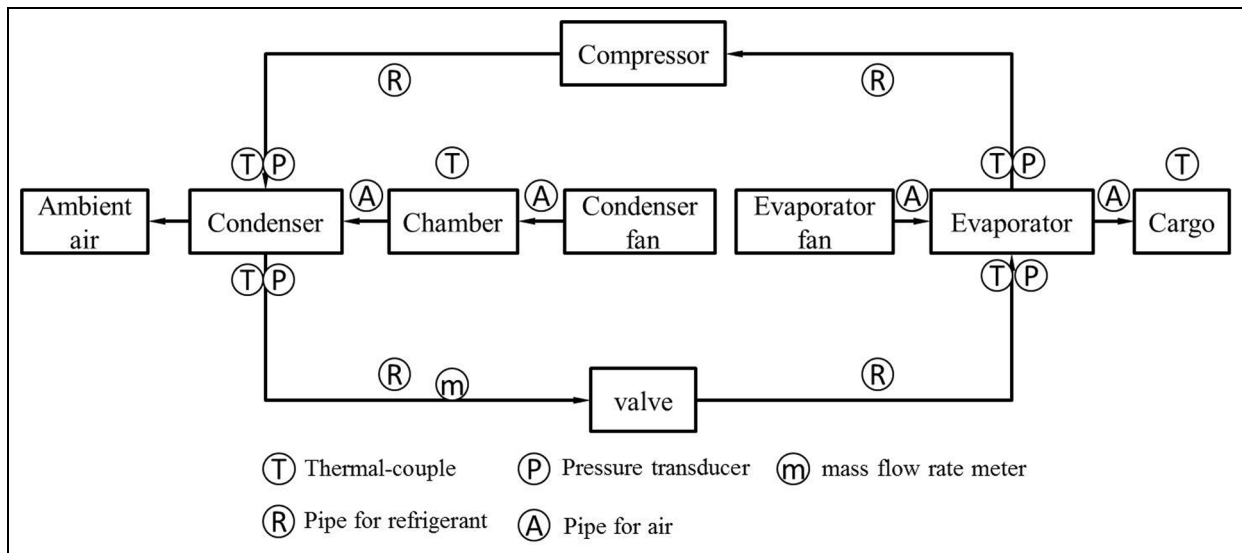


**Figure 5.** Schematic diagram of the whole experimental set-up.

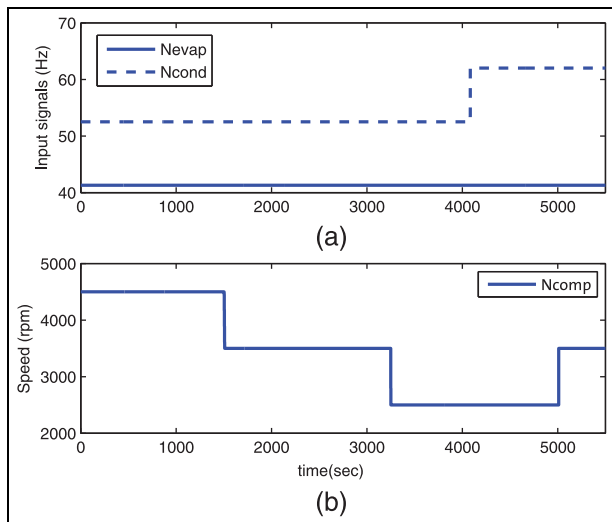


**Figure 6.** Inputs of the system: (a) input signals of two heat exchanger fans; (b) compressor speed. rpm: r/min.

simulation work, the initial conditions and the unknown parameters are identified offline by one set of experimental data as stated in the section on parameter identification, and the model is evaluated using the other unseen data. In the following, several other sets of data are used to validate the model by comparing the experimental results and simulation results for three different scenarios.

In the first scenario, the speeds of the condenser fan and the compressor change while the speed of the evaporator fan remains unchanged during the 5500 s simulations, as seen in Figure 6. Figure 7 shows the air temperature at the condenser outlet and the evaporator outlet while the inlet temperatures are measured and fed to the model. The air temperature at the outlet agrees with the test data but with a little discrepancy,

which is probably caused by using the constant refrigerant-side heat transfer coefficient. For more accurate results, in the future, this coefficient should be identified online. In order to keep the superheating at a certain degree, the expansion valve has to be turned down or up. As a result, the real temperature at the evaporator outlet always oscillates. Given that the thermostatic valve model is identified by steady-state data, it is difficult to simulate these oscillations, but this phenomenon can be overcome by the use of dynamic test data in the future. Thus, the simulation results are located in almost the middle of the test data, whereas the simulation results and the test data shown in Figure 8 for the temperature at the inlet match very well. In Figure 9, the simulation results of the refrigerant temperature at the condenser side also fit the test data. Figure 10 demonstrates the good agreement between the actual evaporator and condenser pressures and the model predictions.

In the second scenario, the speeds of the evaporator fan and the compressor are varied and the speed of the condenser fan is constant. From Figure 11 to Figure 15, conclusions similar to those from the first scenario can be drawn during the 2500 s simulations.

In the last scenario, the input pattern is more complex; at the 560th second, three inputs were changed, as depicted in Figure 16. However, from Figure 17 to Figure 20, it can be seen that the simulation results also fit the test data but, because of the highly non-linear nature of the system, any system parameter can be affected by each of the three inputs. If we take the evaporator pressure in Figure 20 as an example, it can be seen that it is influenced by both  $N_{evap}$  and  $N_{comp}$ . The pressure increases as  $N_{comp}$  decreases, and it decreases as  $N_{evap}$  decreases. That is why, at the 560th second, the evaporator pressure does not change very much. In Figure 18, the refrigerant temperatures are closely

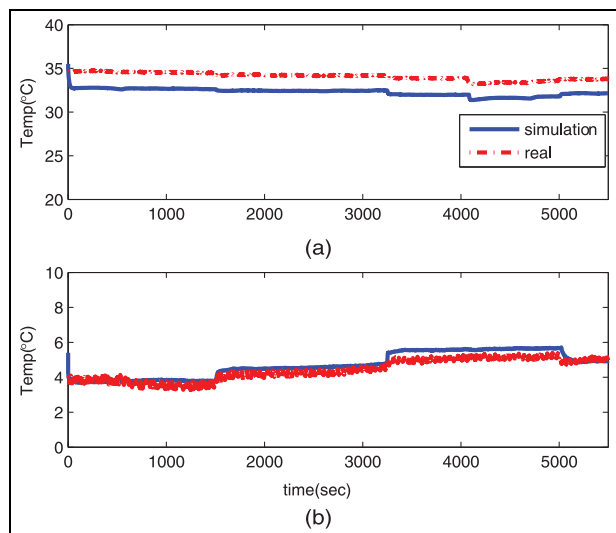


**Figure 7.** Air temperatures at (a) the outlet of the condenser and (b) the outlet of the evaporator. Temp: temperature.

related to the evaporator pressure. The temperature at the evaporator inlet is the saturation temperature under the evaporator pressure, and the temperature at the evaporator outlet is the sum of the saturation temperature and the superheat temperature. That is why they remain fairly constant when the inputs are changed.

The comparison results are given in the form of the mean absolute percentage error (MAPE) in Table 2, which is the average value for the three scenarios. From the results, it can be seen that the model prediction is accurate and can be used in the development of the model predictive controller.

### Development of the controller

In order to show further that the proposed model has sufficient accuracy to be utilized for controller development and can serve as a basis to evaluate other controllers, the on-off controller is developed first, and its simulation results and experimental results are compared. Because of its simplicity and because it is easy to apply, the on-off controller is popular and extensively used currently. However, its nature also leads to the following disadvantages. First, it is unable to regulate the temperature oscillation amplitudes upon changing conditions, such as the ambient temperature and any varying food temperature requirements, and so it may amplify food deterioration or make people feel uneasy. Second, frequent compressor on-off activations can lead to excessive power consumption and cause mechanical components to wear over time.<sup>5</sup> More importantly, energy saving is not considered in the on-off controller, which is the reason to develop more advanced controllers for automotive A/C-R systems.

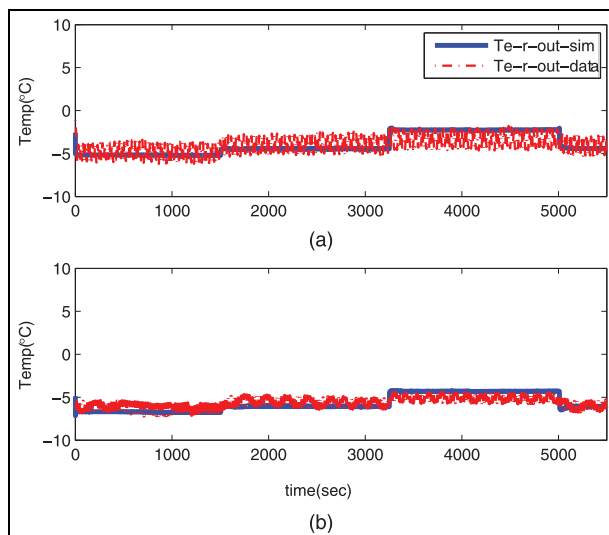


**Figure 8.** Refrigerant temperatures at (a) the inlet of the evaporator and (b) the outlet of the evaporator. Temp: temperature.

### On-off controller

For the controller application, the model of the evaporator-side chamber should be integrated into the A/C-R system models. From Figure 5, it can be seen that the chamber used is a 2 m<sup>3</sup> wooden chamber to represent the cargo for a truck. The inside air temperature of the cargo is one of the control objectives the dynamics of which are given approximately by

$$\frac{dT_{cargo}}{dt} = \frac{\dot{Q}_{inconv} + \dot{Q}_{inf} + \dot{Q}_{door} - \dot{Q}_{vecc}}{(MC)_{air}} \quad (15)$$

where  $\dot{Q}_{inconv}$  is the convective heat transfer from the interior surface,  $\dot{Q}_{door}$  is the extra load due to opening the door during delivery,  $\dot{Q}_{inf}$  is the extra load due to the infiltration load and  $\dot{Q}_{vecc}$  is the cooling capacity produced by the A/C-R systems to balance the heating load from outside.<sup>15</sup> In the simulations and experimental work, the first two parameters are treated together and identified by test data as the heating load from outside.  $\dot{Q}_{door}$  as the extra heating load or the disturbance is added to the experimental process by a heater.  $(MC)_{air}$  is the thermal inertia of the air inside the whole cargo space.

The following logic rules can be employed to demonstrate the basic idea.

1. If the current evaporator-side chamber temperature is higher than the upper band, the compressor will be turned on.
2. If the current evaporator-side chamber temperature is lower than the lower band, the compressor will be shut down.
3. If the current evaporator-side chamber temperature is between the upper band and the lower band, the compressor state will remain unchanged.

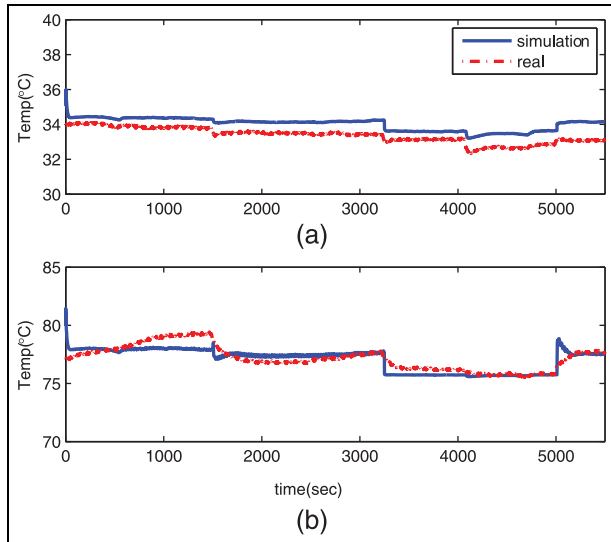


**Figure 9.** Refrigerant temperatures at (a) the inlet of the condenser and (b) the outlet of the condenser. Temp: temperature.

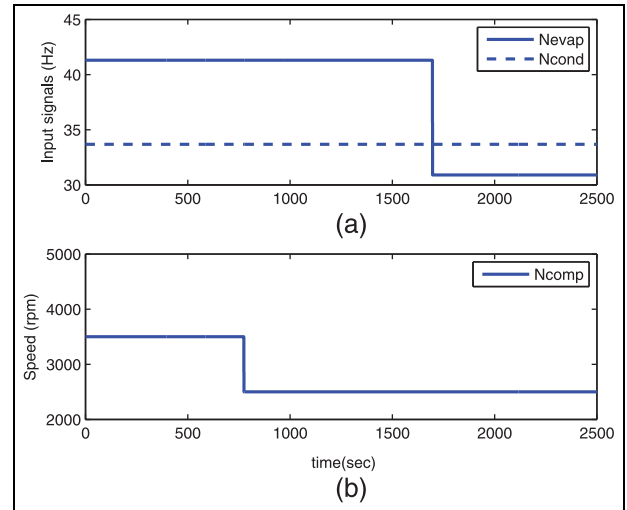


**Figure 11.** Inputs of the system: (a) input signals of two heat exchanger fans; (b) compressor speed. rpm: r/min.

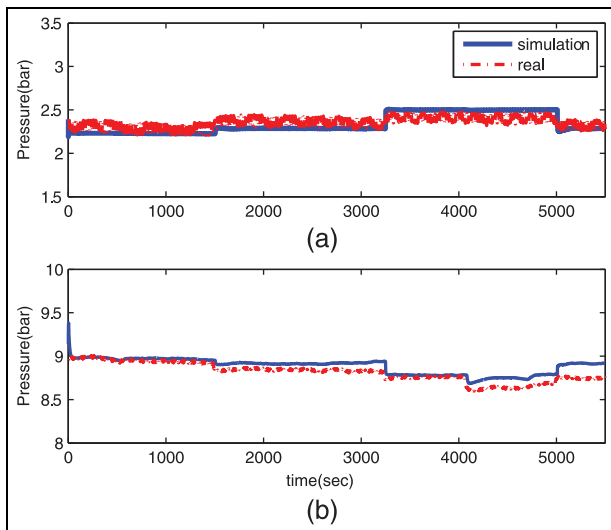


**Figure 10.** Pressures of (a) the evaporator and (b) the condenser.

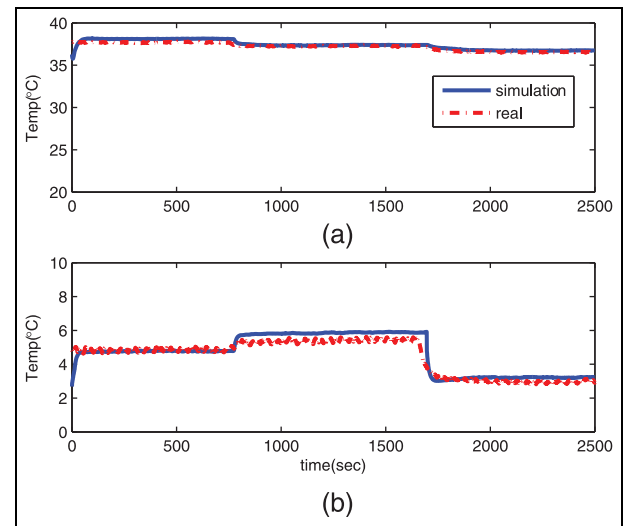


**Figure 12.** Air temperatures at (a) the outlet of the condenser and (b) the outlet of the evaporator. Temp: temperature.

The operating conditions and the initial values of some parameters for the two scenarios are listed in Table 3. From Figure 21 and Figure 22, it can be seen that the simulation results are in agreement with the experimental tests. This also shows the accuracy of the model. In addition, this model can run about 30 times faster than in real time on a regular computer compared with the 1.56 times proposed by Shah et al.<sup>18</sup>

**Development of a discrete model predictive controller**

As is known, A/C-R systems are highly non-linear multiple-input multiple-output systems with slow dynamics. If the non-linear system model is directly

used for a model predictive controller design, its computational efficiency is extremely low so that the non-linear model predictive controller cannot be implemented as a real-time microcontroller. To solve this problem, a linear model predictive controller is developed in this paper. The whole procedure, including model linearization, discretization and objective function reformulation, has been described in detail by Borrelli et al.<sup>29</sup> The main idea is that an optimization problem should be solved at each time instant. By introducing a prediction of the horizon length  $N$ , the discretized objective function in the next  $N$  steps is formulated according to

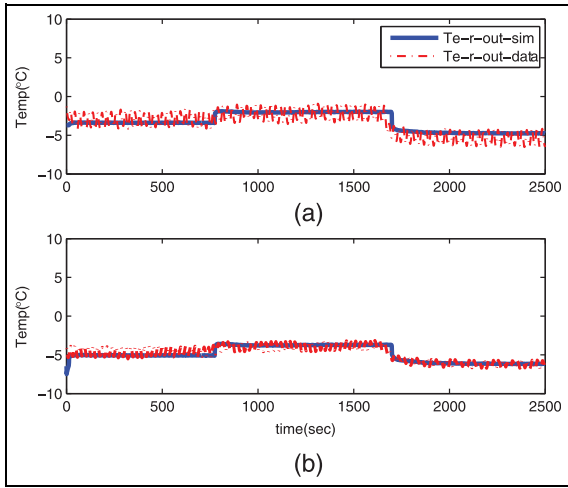


**Figure 13.** Refrigerant temperatures at (a) the inlet of the evaporator and (b) the outlet of the evaporator. Temp: temperature.

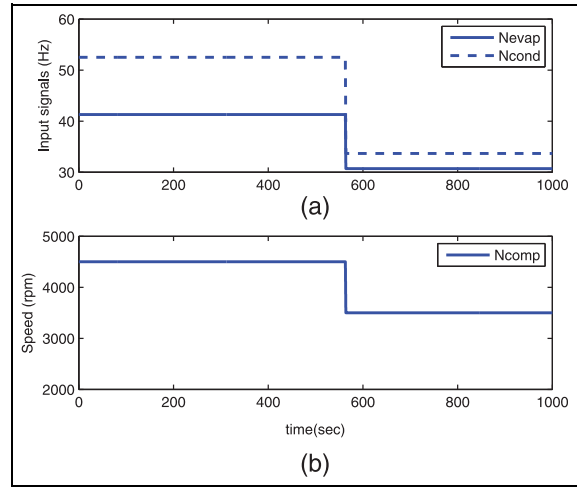


**Figure 16.** Inputs of the system: (a) input signals of two heat exchanger fans; (b) compressor speed. rpm: r/min.

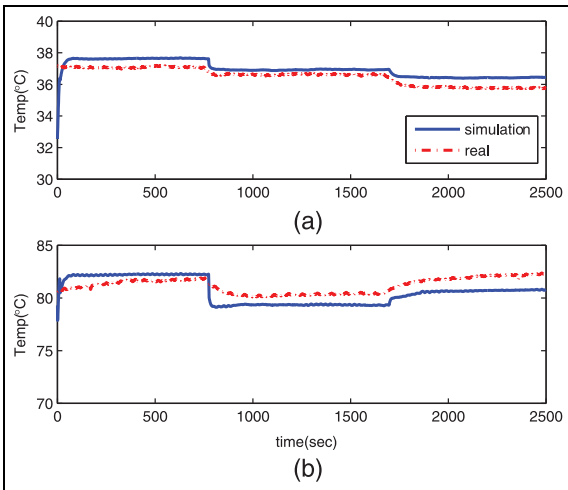


**Figure 14.** Refrigerant temperatures at (a) the inlet of the condenser and (b) the outlet of the condenser. Temp: temperature.

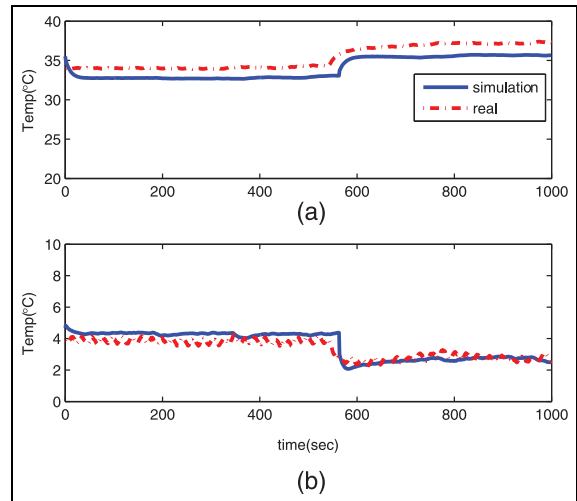


**Figure 17.** Air temperatures at (a) the outlet of the condenser and (b) the outlet of the evaporator. Temp: temperature.

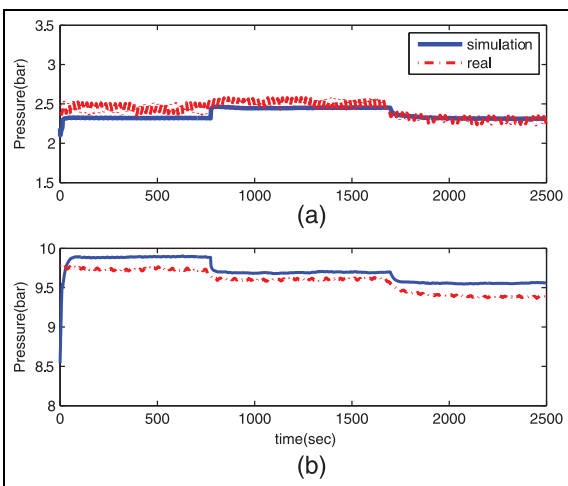


**Figure 15.** Pressures of (a) the evaporator and (b) the condenser.

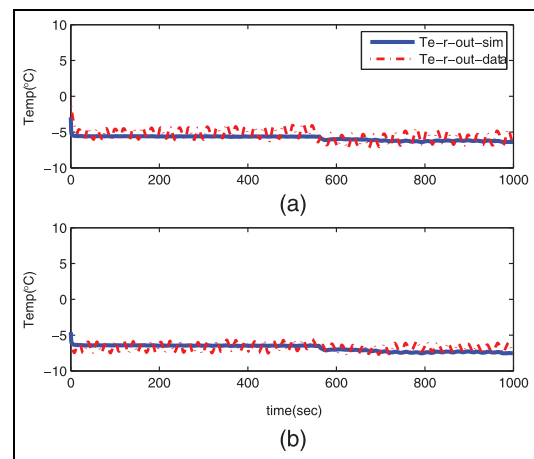


**Figure 18.** Refrigerant temperatures at (a) the inlet of the evaporator and (b) the outlet of the evaporator. Temp: temperature.

**Table 2.** The MAPE between the simulations and the test data.

| Parameter   | MAPE (%) |
|---|----------|
| Pressure of the evaporator                              | 2.77     |
| Pressure of the condenser                               | 1.06     |
| Temperature of the refrigerant at the condenser outlet  | 1.66     |
| Temperature of the refrigerant at the condenser inlet   | 0.96     |
| Temperature of the refrigerant at the evaporator outlet | 8.66     |
| Temperature of the refrigerant at the evaporator inlet  | 8.43     |
| Temperature of the air at the evaporator outlet         | 8.69     |
| Temperature of the air at the condenser outlet          | 3.27     |

MAPE: mean absolute percentage error.

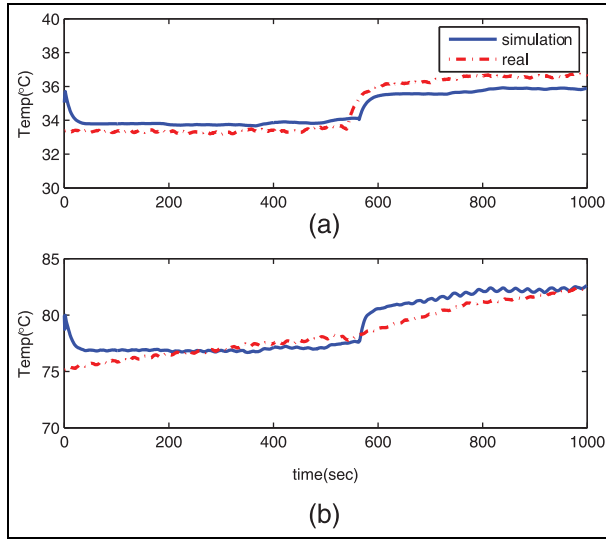


**Figure 19.** Refrigerant temperatures at (a) the inlet of the condenser and (b) the outlet of the condenser. Temp: temperature.

$$J(x_0, u_0) = e(N)^T P e(N) + \sum_{k=0}^{N-1} e(k)^T Q e(k) + \Delta u(k)^T S \Delta u(k)$$

with

$$e(k) = y(k) - y_{ref}(k), k = 1, 2, \dots, N$$

s.t.

$$x_{min} \leq x(k) \leq x_{max}$$

$$u_{min} \leq u(k) \leq u_{max}$$

$$\Delta u_{min} \leq \Delta u(k) \leq \Delta u_{max}$$

where the first item, namely the final state costs, and the last item, namely the increments in the inputs, are added to the above function in order to make the controller more stable. Furthermore, the optimization problem is always subjected to some constraints. Finally, the objective function (equation (18)) of this

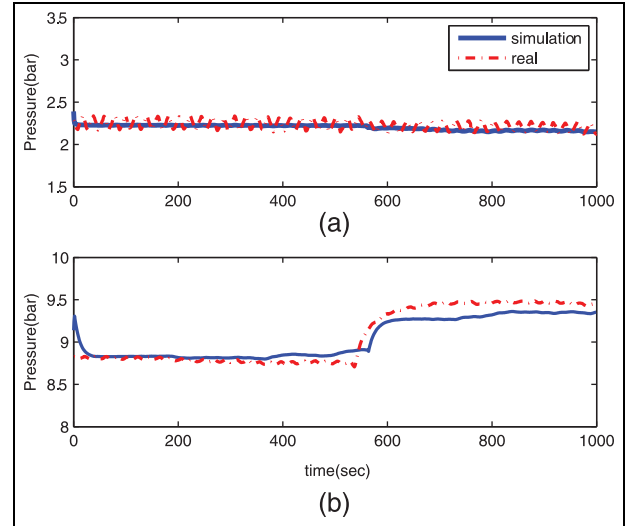


**Figure 20.** Pressures of (a) the evaporator and (b) the condenser.

**Table 3.** Operating and initial conditions.

| Parameter (units)  | Value for the following |            |
|--|-------------------------|------------|
|  | Scenario 1              | Scenario 2 |
| Ambient temperature (°C)                                       | 25                      | 25         |
| Initial temperature of the evaporator side of the chamber (°C) | 23                      | 23         |
| Temperature set point (°C)                                     | 16                      | 17         |
| Heating load (kW)  | 0.65                    | 0.65       |
| Extra heating from the door opening (kW)                       | 0.15                    | 0.15       |
| Speed of the evaporator fan (Hz)                               | 40                      | 40         |
| Speed of the condenser fan (Hz)                                | 40                      | 40         |
| Speed of the compressor pump (r/min)                           | 4500                    | 4500       |

tracking problem is transferred into quadratic form with respect to the increment in the control inputs in preparation for using the convex quadratic programming problem solver.<sup>30</sup> The convex quadratic objective function only with respect to the increment in the input item is obtained by using the linearized and discretized system model and reformulating the original objective function shown in equation (18) by

$$J(x_0, u_0) = \frac{1}{2} \Delta \bar{U}^T H \Delta \bar{U} + \Delta \bar{U}^T g$$

s.t.

$$\Delta \bar{U} \geq \max(\Delta \bar{U}_{min}(U), \Delta \bar{U}_{min}(\Delta \bar{U}), \Delta \bar{U}_{min}(X))$$

$$\Delta \bar{U} \leq \min(\Delta \bar{U}_{max}(U), \Delta \bar{U}_{max}(\Delta \bar{U}), \Delta \bar{U}_{max}(X))$$

where the Hessian matrix  $H$  is symmetric and positive or semipositive definite and  $g$  is the gradient vector. The constraints shown in equation (18) are also

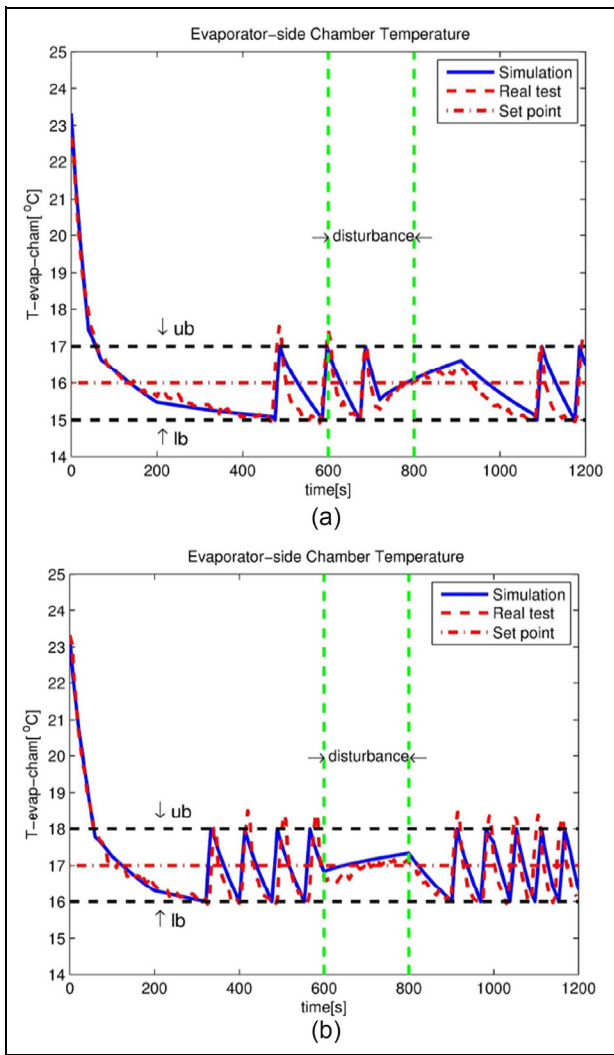


**Figure 21.** Controlled temperature performances: (a) scenario 1; (b) scenario 2.

reformulated into constraints only related to the increments in the system inputs. After solving the above problem, the first element of the optimal solution is applied to the real system. This linear model predictive controller is constructed in MATLAB/Simulink and its structure is shown in Figure 23, where look-up tables are used to implement the thermodynamic properties of the refrigerant. Then, several unknown parameters are identified and sent to the algorithm and the solver together with all other known information.

In this linear model predictive controller, the constraints of the system inputs and the controller parameters are shown in Table 4, where the time step length  $T_s$  is used for simulations while the actual time used for one step simulation is only 0.04 s on a regular computer, which is sufficiently fast for real-time implementation.

Because of the existence of the discrete input compressor speed, a discrete model predictive controller

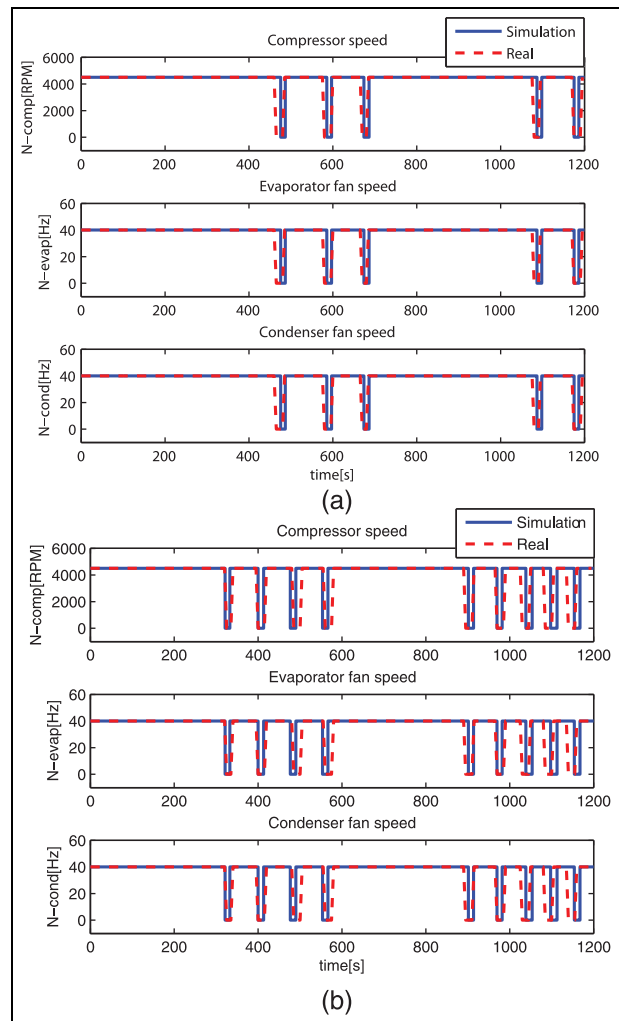


**Figure 22.** System inputs: (a) scenario 1; (b) scenario 2. RPM: r/min.

is developed, which is composed of three submodel predictive controllers, as shown in Figure 24. Three submodel predictive controllers are running simultaneously at three different compressor speeds (2500 r/min, 3500 r/min and 4500 r/min) to find the optimal solutions of the other two inputs. Then, the three best cost values are recalculated by the two optimal input values as well as the corresponding compressor speeds. By comparing their values, the minimum value is the optimal cost of the current time instant, and the corresponding input values are the optimal solution. For example, if  $J_{3500}$  is the minimum cost value, then the optimal solution is the combination of  $N_{comp} = 3500$  r/min as well as the optimal values of  $N_{evap}$  and  $N_{cond}$  found for the submodel predictive controller at 3500 r/min.

The simulation results are presented in Figure 25 and Figure 26. It can be seen from the results that the chamber temperature quickly settles and stays at that level. For a period of large disturbance caused by an



**Table 4.** Inputs constraints and linear parameter values of the model predictive controller.

| $N_{comp}$ (r/min)                                   | $N_{evap}$ (Hz) | $N_{cond}$ (Hz) | $T_s$ (s) | $Q$     | $N$ | $P$   | $R$   | $S$   |
|--|-----------------|-----------------|-----------|---------|-----|-------|---|---|
| $\begin{bmatrix} 2500 \\ 3500 \\ 4500 \end{bmatrix}$ | $[0-40]$        | $[0-40]$        | 5         | 100,000 | 10  | 1000Q | $\begin{bmatrix} 5 & 0 & 0 \\ 0 & 0 & 0 \\ 0 & 0 & 0 \end{bmatrix}$ | $\begin{bmatrix} 0 & 0 & 0 \\ 0 & 1000 & 0 \\ 0 & 0 & 1000 \end{bmatrix}$ |

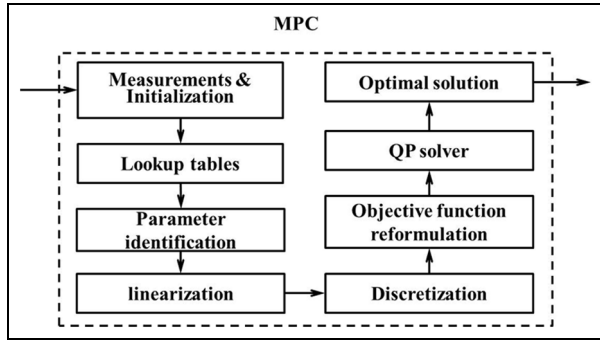


**Figure 23.** Structure of the model predictive controller. QP: quadratic programming.

extra heating load, the controller tries to maintain the temperature at its set point by increasing the speed of the evaporator fan as well as the speed of the condenser fan instead of changing the compressor speed, which is mainly related to the energy consumption. That is why a large weight was chosen for the increment in the compressor speed. This weight should be decreased or  $Q$  should be increased if more emphasis is put on the temperature performance. The simulation time for the model predictive controller is much shorter than real time, which means that this controller can be applied in the real control system.

**Comparison**

In order to demonstrate the advantage of the model predictive controller, the results of the on-off controller and the model predictive controller are compared from several viewpoints by using the MAPE.

Obviously, the temperature performance of the model predictive controller is better than that of the conventional on-off controller not only during the dynamic period but also in the steady-state region from the above figures. By data analysis, the values in Table 5 can demonstrate a more convincing conclusion that both the set-point controller and the model predictive controller have better performances than the two conventional controllers. More specifically, the first MAPE measures the deviation between the real temperature responses and the simulation temperature responses. The small MAPE values mean that the model used for development of the controller has a high accuracy. The second MAPE demonstrates the offset between the temperature response and its set

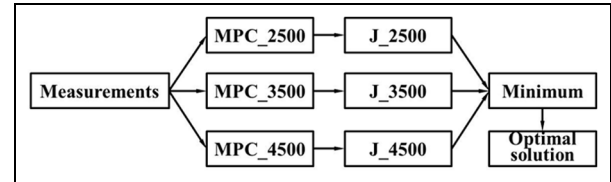


**Figure 24.** Structure of the discrete model predictive controller.

MPC\_2500: model predictive controller at 2500 r/min; MPC\_3500: model predictive controller at 3500 r/min; MPC\_4500: model predictive controller at 4500 r/min; J\_2500: minimum cost value at 2500 r/min; J\_3500: minimum cost value at 3500 r/min; J\_4500: minimum cost value at 4500 r/min.

point, whereas the maximum absolute percentage error shows the largest drift of the temperature from its set point. It can be seen that the on-off controller has a worse performance than the model predictive controller has.

**Conclusions**

The goal of this study was to design an advanced energy efficient controller for automotive A/C-R systems to provide benefits for both vehicle owners and the environment.

First, a control-based model was developed that not only reflects the dominant dynamics of A/C-R systems but also was sufficiently simple to be used in real-time controllers. The model is a trade-off between the accuracy of a full detailed thermodynamics model and the simplicity needed for a real-time controller. The proper modelling of heat exchangers is vitally important in representing the overall dynamics of A/C-R systems. The effects of fins in the heat transfer process of heat exchangers were considered to improve the accuracy of A/C-R models. The effects of the fins were lumped into the equivalent parameters to keep the simplicity of the model. The parameters, however, can be identified directly from experimental data. Unlike the existing model, the effects from the superheated section of the condenser were also integrated into the proposed model to guarantee its accuracy. Then, the experimental analysis shows that the model can correctly predict the complex behaviour of A/C-R systems. Because of its simplicity, it can be easily used in real-time controllers.

Finally, to demonstrate its accuracy further and to achieve its optimal performance, a popularly used on-

**Table 5.** Comparison of the results of the controllers.

| Controller performance                             | Scenario 1 |                             | Scenario 2 |                             |
|--|------------|-----------------------------|------------|-----------------------------|
|  | On-off     | Model predictive controller | On-off     | Model predictive controller |
| MAPE between the real tests and the simulations(%) | 1.6        | 3.14                        | 1.92       | 1.72                        |
| MAPE between the simulations and the set point (%) | 4.36       | 3.37                        | 4.20       | 3.00                        |
| Maximum absolute percentage error (%)              | 9.63       | 5.76                        | 8.9        | 5.91                        |
| Controller performance                             | Bad        | Good                        | Bad        | Good                        |
| Energy consumption (kW h for 1200 s)               | 0.2063     | 0.1902                      | 0.2041     | 0.1793                      |
| Improvement in the energy (%)                      | 0          | 7.8                         | 0          | 10.33                       |

MAPE: mean absolute percentage error.

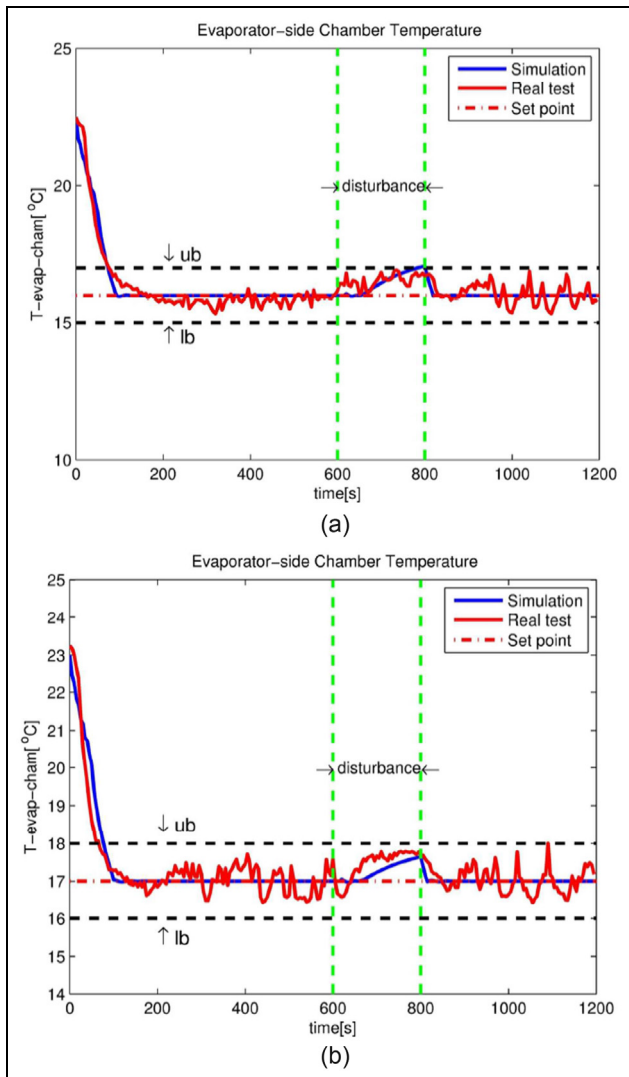


**Figure 25.** Controlled temperature performances: (a) scenario 1; (b) scenario 2..

off controller was designed, which also serves as a basis for comparison with other controllers. Simulations and experimental results showed that the proposed discrete model predictive controller is capable of improving the

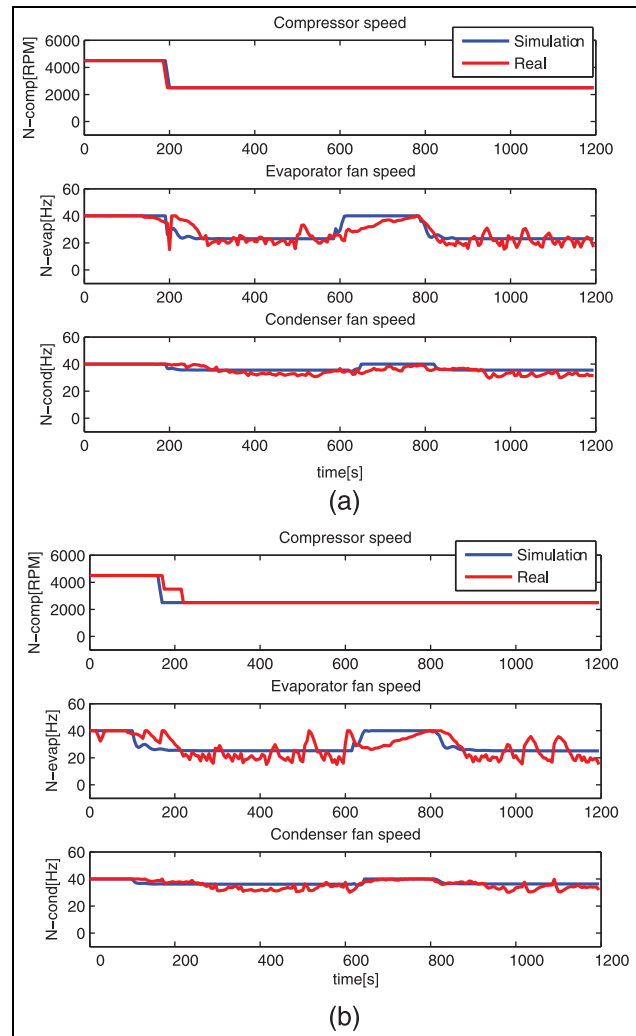


**Figure 26.** System inputs: (a) scenario 1; (b) scenario 2. RPM: r/min.

performance of controlled temperature while saving about 8% energy compared with the conventional controller under the examined scenario. The proposed model predictive controller can result in more fuel savings to the owners as well as to the environment.

## Acknowledgements

The authors would like to acknowledge the technical support of Automotive Partnership Canada and the Cool-it Group.

## Declaration of conflicting interests

The author(s) declared no potential conflicts of interest with respect to the research, authorship, and/or publication of this article.

## Funding

The author(s) disclosed receipt of the following financial support for the research, authorship, and/or publication of this article: This work was supported by the Automotive Partnership Canada and the Cool-it Group.

## References

- Dinçmen E and Güvenç BA. A control strategy for parallel electric vehicles based on extreme seeking. *Veh System Dynamics* 2012; 50(2): 199–227.
- Lust EE. *System-level analysis and comparison of long-haul truck idle-reduction technologies*. MSc Thesis, University of Maryland, College Park, Maryland, USA, 2008.
- Morshed MR. *Unnecessary idling of vehicles: an analysis of the current situation and what can be done to reduce it*. MSc Thesis, McMaster University, Hamilton, Ontario, Canada, 2010.
- Khayyama H, Nahavandia S, Hub E et al. Intelligent energy management control of vehicle air conditioning via look-ahead system. *Appl Thermal Engng* 2011; 16: 3147–3160.
- Liu JY, Zhou HL and Zhou XG. Automotive air conditioning control – a survey. In: *International conference on electronic and mechanical engineering and information technology*, Harbin, Heilongjiang, People's Republic of China, 12–14 August, 2011, pp. 3408–3412. New York: IEEE.
- Chiara F and Canova M. A review of energy consumption, management, and recovery in automotive systems, with considerations of future trends. *Proc IMechE Part D: J Automobile Engineering* 2013; 227(6): 914–936.
- Budde-Meiwes H, Drillkens J, Lunz B and Muennix J. A review of current automotive battery technology and future prospects. *Proc IMechE Part D: J Automobile Engineering* 2013; 227(5): 761–776.
- Johri R and Filipi Z. Optimal energy management of a series hybrid vehicle with combined fuel economy and low-emission objectives. *Proc IMechE Part D: J Automobile Engineering* 2014; 228(12): 1424–1439.
- Jalaliyazdi M, Khajepour A, Chen S and Litkouhi B. Handling delays in stability control of electric vehicles using MPC. SAE paper 2015-01-1598, 2015.
- Kania M, Koeln J, Alleyne A et al. A dynamic modeling toolbox for air vehicle vapor cycle systems. SAE paper 2012-01-2172, 2012.
- He XD. *Dynamic modeling and multivariable control of vapor compression cycles in air conditioning systems*. PhD thesis, Massachusetts Institute of Technology, Cambridge, Massachusetts, USA, 1996.
- MacArthur JW and Grald EW. Unsteady compressible two-phase flow model for predicting cyclic heat pump performance and a comparison with experimental data. *Int J Refrig* 1989; 12(1): 29–41.
- Rasmussen BP and Alleyne AG. Dynamic modeling and advanced control of air conditioning and refrigeration systems. ACRC Technical Report 244, Air Conditioning and Refrigeration Center, University of Illinois, Urbana, Illinois, USA, 2006.
- Wedekind GL, Bhatt BL and Beck BT. A system mean void fraction model for predicting various transient phenomena associated with two-phase evaporating and condensing flows. *Int J Multiphase Flow* 1978; 4: 97–114.
- Li B. *Dynamic modeling and control of vapor compression cycle systems with shut-down and start-up operations*. MS Thesis, University of Illinois at Urbana–Champaign, Champaign, Illinois, USA, 2009.
- Eldredge BD and Alleyne AG. Improving the accuracy and scope of control-oriented vapor compression cycle system models. ACRC Technical Report 246, Air Conditioning and Refrigeration Center, University of Illinois, USA, 2006.
- Fasl JM. *Modeling and control of hybrid vapor compression cycles*. MS Thesis, University of Illinois at Urbana–Champaign, Champaign, Illinois, USA, 2013.
- Shah R, Alleyne AG, Bullard CW et al. Dynamic modeling and control of single and multi-evaporator subcritical vapor compression systems. ACRC Technical Report 216, Air Conditioning and Refrigeration Center, University of Illinois, Urbana, Illinois, USA, 2003.
- Rasmussen BP. *Control-oriented modeling of transcritical vapor compression systems*. MS Thesis, University of Illinois at Urbana-Champaign, Champaign, Illinois, USA, 2002.
- Li B, Jain N, Mohs WF et al. Dynamic modeling of refrigerated transport systems with cooling-mode/heating-mode switch operations. *HVAC&R Res* 2012; 18(5): 974–996.
- McKinley TL and Alleyne AG. An advanced nonlinear switched heat exchanger model for vapor compression cycles using the moving-boundary method. *Int J Refrig* 2008; 31: 1253–1264.
- He XD, Liu S, Asada HH et al. Multivariable control of vapor compression systems. *HVAC&R Res* 2011; 4(3): 205–230.
- Lee J, Kim J, Park J et al. Effect of the air-conditioning system on the fuel economy in a gasoline engine vehicle. *Proc IMechE Part D: J Automobile Engineering* 2013; 227(1): 66–77.
- Dhand A and Pullen K. Optimal energy management for a flywheel-assisted battery electric vehicle. *Proc IMechE Part D: J Automobile Engineering* 2015; 229(12): 1672–1682.
- Refrigerant reference guide*. 4th edition. Philadelphia, Pennsylvania: National Refrigerants, Inc., 2006. <http://www.refrigerants.com/ReferenceGuide2006.pdf>.
- Salim MM. Potential for expanders in a mobile carbon dioxide air-conditioning system. *Proc IMechE Part D: J Automobile Engineering* 2009; 224(2): 219–228.
- Nejad EK, Hajabdollahi M and Hajabdollahi H. Modeling and second law based optimization of plate fin and

- tube heat exchanger using MOPSO. *J Appl Mech Engng* 2012; 2: 1000118.
28. Jabardo JM and Mamani WG. Modeling and experimental evaluation of parallel flow micro channel condensers. *J Braz Soc Mech Sci Engng* 2003; 25(2): 107–114.
29. Borrelli F, Bemporad A and Morari M. *Predictive control*. Draft. 2012. <http://www.mpc.berkeley.edu/mpc-course-material> (in preparation).
30. Ferreau HJ, Arnold E, Buchner A et al. *qpOASES user's manual, version 3.0*. Leuven: KU Leuven, 2014.

## Appendix I

### Notation

|                  |   |                  |   |
|------------------|---|------------------|---|
| $h_{ge}$         | enthalpy of the vapour refrigerant at the evaporator inlet    | $N_{comp}$       | compressor speed  |
| $h_{ic}$         | enthalpy of the refrigerant at the condenser inlet            | $N_{cond}$       | control input of the condenser fan                            |
| $h_{ie}$         | enthalpy of the refrigerant at the evaporator inlet           | $N_{evap}$       | control input of the evaporator fan                           |
| $h_{is}$         | isentropic enthalpy of the refrigerant in the compressor      | $P_c$            | pressure of the condenser                                     |
| $h_{le}$         | enthalpy of the liquid refrigerant at the evaporator inlet    | $P_e$            | pressure of the evaporator                                    |
| $h_{lgc}$        | latent enthalpy of the refrigerant at the condenser inlet     | $Pr$             | Prandtl number for air  |
| $h_{lge}$        | latent enthalpy of the refrigerant at the evaporator inlet    | $S$              | slip ratio  |
| $h_{oc}$         | enthalpy at the condenser outlet                              | $St$             | Stanton number  |
| $j$              | Colburn factor  | $T_a$            | air temperature around the heat exchanger                     |
| $L_c$            | total length of the condenser tube wall                       | $T_{ic}$         | temperature of the refrigerant at the condenser inlet         |
| $L_e$            | total length of the evaporator tube wall                      | $T_{rc}$         | saturation temperature of the refrigerant in the condenser    |
| $m$              | total mass of the heat exchanger                              | $T_{re}$         | saturation temperature of the refrigerant in the evaporator   |
| $\dot{m}_{comp}$ | mass flow rate of the refrigerant through the compressor      | $T_{sh}$         | temperature in the superheated section                        |
| $m_{pipe}$       | total mass of the refrigerant in the pipes                    | $V_d$            | volumetric displacement of the compressor                     |
| $\dot{m}_v$      | mass flow rate of the refrigerant through the expansion valve | $\bar{\gamma}_c$ | mean void fraction of the two-phase section of the condenser  |
|                  |   | $\bar{\gamma}_e$ | mean void fraction of the two-phase section of the evaporator |
|                  |   | $\eta_a$         | adiabatic efficiency of the compressor                        |
|                  |   | $\eta_{vol}$     | volumetric efficiency of the compressor                       |
|                  |   | $\rho_{gc}$      | density of the vapour refrigerant in the condenser            |
|                  |   | $\rho_{ge}$      | density of the vapour refrigerant in the evaporator           |
|                  |   | $\rho_{lc}$      | density of the liquid refrigerant in the condenser            |
|                  |   | $\rho_{le}$      | density of the liquid refrigerant in the evaporator           |
|                  |   | $\rho_{ref}$     | density of the refrigerant                                    |
|                  |   | $\rho_v$         | density of the refrigerant through the valve                  |

## Appendix 2

The complete non-linear and linearized models at the current operating point are given in Table 6.

**Table 6.** The complete non-linear and linearized models.

|  |  |           |   |
|--|--|-----------|---|
| $\dot{x}$  | $f(x, u)$  | $f_{12x}$ | $\left( \dot{m}_v \frac{dh_{ge}}{dP_e} + \alpha_i A_i \frac{l_e}{L_e} \frac{dT_{re}}{dP_e} \right) / [\rho_{ie} h_{ige} A_e (1 - \bar{\gamma}_e)]$      |
| $y$  | $g(x, u)$  | $f_{13x}$ | $-\frac{\rho_{ie} h_{ige} A_e (1 - \bar{\gamma}_e) L_e}{\alpha_i A_i l_e}$  |
| $u$  | $[N_{comp}, N_{evap}, N_{cond}]^T$   | $f_{22x}$ | $\left( \dot{m}_v \frac{dh_{ie}}{dP_e} - \alpha_i A_i \frac{l_e}{L_e} \frac{dT_{re}}{dP_e} \right) / h_{ige} A_e L_e \frac{d\rho_{ge}}{dP_e}$           |
| $x$  | $[l_e, P_e, T_{we}, P_c, T_{wc}, T_{cargo}]^T$   | $f_{23x}$ | $\alpha_i A_i l_e / h_{ige} A_e L_e^2 \frac{d\rho_{ge}}{dP_e}$  |
| $y$  | $T_{cargo}$  | $f_{24x}$ | $\dot{m}_v \frac{dh_{ie}}{dP_c} / h_{ige} A_e L_e \frac{d\rho_{ge}}{dP_e}$  |
| $f = \begin{bmatrix} f_1 \\ f_2 \\ f_3 \\ f_4 \\ f_5 \\ f_6 \end{bmatrix}$ | $\begin{bmatrix} \frac{\dot{m}_v (h_{ge} - h_{ie}) - \alpha_{ie} \pi D_{ie} l_e (T_{wfe} - T_{re})}{\rho_{ie} h_{ige} A_e (1 - \bar{\gamma}_e)} \\ \left[ \dot{m}_v \frac{h_{ie} - h_{le}}{h_{ige}} - \dot{m}_{comp} + \frac{\alpha_{ie} \pi D_{ie} l_e (T_{wfe} - T_{re})}{h_{ige}} \right] / A_e L_e \frac{d\rho_{ge}}{dP_e} \\ \frac{\alpha_{oc} A_{oc} (T_{ae} - T_{wfe}) - \alpha_{ie} \pi D_{ie} l_e (T_{wfe} - T_{re}) - \alpha_{iesh} \pi D_{ie} (L_e - l_e) (T_{wfe} - T_{re})}{(C_p m)_{we}} \\ \left[ \dot{m}_{com} - \frac{\alpha_{ic} \pi D_{ic} l_c (T_{rc} - T_{wc})}{h_{igc}} \right] / A_c L_c \frac{d\rho_{gc}}{dP_c} \\ \left[ \dot{m}_{comp} - \frac{\alpha_{ic} \pi D_{ic} l_c (T_{rc} - T_{wfc})}{h_{igc}} \right] / (C_p m)_{wc} \\ \frac{\dot{Q}_{out} - \alpha_o A_o l_e (T_a - T_{we})}{(MC)_{air}} \end{bmatrix}$ | $f_{32x}$ | $\alpha_i A_i \frac{dT_{re}}{dP_e} / (C_p m)_{we}$  |
| $g(x, u)$  | $x_6$  | $f_{33x}$ | $-\alpha_i A_i + \alpha_o A_o \left( \frac{dT_a}{dT_{we}} - 1 \right) / (C_p m)_{we}$   |
| $A_e$  | $\begin{bmatrix} f_{11x} & f_{12x} & f_{13x} & f_{14x} & 0 & 0 \\ f_{21x} & f_{22x} & f_{23x} & f_{24x} & 0 & 0 \\ 0 & f_{32x} & f_{33x} & 0 & f_{35x} & 0 \\ f_{41x} & 0 & 0 & f_{44x} & f_{45x} & 0 \\ 0 & 0 & 0 & f_{54x} & f_{55x} & 0 \\ f_{61x} & 0 & f_{63x} & 0 & 0 & f_{66x} \end{bmatrix}$   | $f_{36x}$ | $\alpha_o A_o \frac{dT_a}{dT_{cargo}} / (C_p m)_{we}$   |
| $B_e$  | $\begin{bmatrix} f_{11u} & 0 & 0 \\ f_{21u} & f_{22u} & 0 \\ 0 & 0 & f_{33u} \\ 0 & f_{42u} & 0 \\ 0 & 0 & 0 \\ 0 & 0 & f_{63u} \end{bmatrix}$   | $f_{41x}$ | $-\alpha_{ic} A_{ic} (T_{rc} - T_{wc}) \partial l_c / \partial l_e / h_{igc} A_c L_c^2 \frac{d\rho_{gc}}{dP_c}$   |
| $C_e$  | $[0 \ 0 \ 0 \ 0 \ 0 \ 0 \ 1]$  | $f_{44x}$ | $-\alpha_{ic} A_{ic} l_c \frac{dT_{rc}}{dP_c} / h_{igc} A_c L_c^2 \frac{d\rho_{gc}}{dP_c}$  |
| $f_{11x}$  | $\frac{\alpha_i A_i (T_{we} - T_{re})}{\rho_{ie} h_{ige} A_e (1 - \bar{\gamma}_e) L_e}$  | $f_{45x}$ | $\alpha_{ic} A_{ic} l_c / h_{igc} A_c L_c^2 \frac{d\rho_{gc}}{dP_c}$  |
|  |  | $f_{54x}$ | $\alpha_{ic} A_{ic} \frac{dT_{rc}}{dP_c} / (C_p m)_{wc}$  |
|  |  | $f_{55x}$ | $-\alpha_{ic} A_{ic} + \alpha_{oc} A_{oc} \left( \frac{dT_{oc}}{dT_{wc}} - 1 \right) / (C_p m)_{wc}$  |
|  |  | $f_{61x}$ | $-\frac{\alpha_o A_o (T_a - T_{we})}{(MC)_{air}}$   |
|  |  | $f_{63x}$ | $-\alpha_o A_o l_e \left( \frac{dT_a}{dT_{we}} - 1 \right) / (MC)_{air}$  |
|  |  | $f_{66x}$ | $-\alpha_o A_o l_e \left( \frac{dT_a}{dT_{cargo}} \right) / (MC)_{air}$   |
|  |  | $f_{11u}$ | $-(h_{ie} - h_{ge}) \frac{d\dot{m}_v}{du_v} / \rho_{ie} h_{ige} A_e (1 - \bar{\gamma}_e)$   |
|  |  | $f_{21u}$ | $\frac{h_{ie} - h_{le}}{h_{ige}} \frac{d\dot{m}_v}{du_v} / A_e L_e \frac{d\rho_{ge}}{dP_e}$   |
|  |  | $f_{22u}$ | $-\frac{d\dot{m}_{comp}}{dN_{comp}} / A_e L_e \frac{d\rho_{ge}}{dP_e}$  |
|  |  | $f_{33u}$ | $\left[ \frac{d\alpha_o}{dN_{evap}} A_o (T_a - T_{we}) + \alpha_o A_o \frac{dT_a}{d\alpha_o} \frac{d\alpha_o}{dN_{evap}} \right] / (C_p m)_{we}$        |
|  |  | $f_{42u}$ | $\frac{d\dot{m}_{comp}}{dN_{comp}} / A_c L_c \frac{d\rho_{gc}}{dP_c}$   |
|  |  | $f_{63u}$ | $\left[ -\frac{d\alpha_o}{dN_{evap}} A_o l_e (T_a - T_{we}) - \alpha_o A_o l_e \frac{dT_a}{d\alpha_o} \frac{d\alpha_o}{dN_{evap}} \right] / (MC)_{air}$ |